The Astrophysical Journal, 938:90 (12pp), 2022 October 20 https://doi.org/10.3847/1538-4357/ac9281

Quantification of the Cross-helicity Turbulent Cascade in Compressible MHD Simulations

Victor Montagud-Camps[1], Petr Hellinger[1], Andrea Verdini[2,3], Emanuele Papini[2,4], Luca Franci[5], and Simone Landi[2,3]
[1] Astronomical Institute, Czech Academy of Sciences, Bocni II/ 1401, CZ-14100 Prague, Czech Republic; victor.montagud-camps@asu.cas.cz
[2] INAF, Osservatorio Astrofisico di Arcetri, Largo E. Fermi 5, I-50125 Firenze, Italy
[3] Università di Firenze, Dipartimento di Fisica e Astronomia, Firenze, Italy
[4] Instituto di Astrofisica e Planetologia Spaziali, via del Fosso del Cavaliere 100, I-00133 Roma, Italy
[5] School of Physical and Chemical Sciences, Queen Mary University of London, London E1 4NS, UK
Received 2022 June 21; revised 2022 August 19; accepted 2022 September 14; published 2022 October 17

Abstract

In plasma turbulence, energy and cross helicity are transferred across scales at a constant rate as a consequence of nonlinear interactions. In incompressible magnetohydrodynamics (MHD), the energy cascade rate of both quantities can be computed by means of the temporal evolution of second-order structure functions, known as Karman–Howarth–Monin (KHM) equations. In the present work, we derive the KHM equation to compute the energy cascade rate of cross helicity in compressible MHD. Using three-dimensional direct numerical simulations, we validate the equation and use it to measure the cross-helicity turbulence properties. Our results show a slower development of the cross-helicity cascade with respect to the energy one and the presence of inverse cascades of energy and cross helicity at large scales when in the presence of a strong mean field. We propose the relation of these phenomena with the longer duration of geomagnetic storms after the arrival of solar winds with large cross helicity and the observation of patchy inertial ranges displaying positive and negative cascade rates for certain solar wind intervals.

Unified Astronomy Thesaurus concepts: Interplanetary turbulence (830); Solar wind (1534); Magnetohydrodynamical simulations (1966); Heliosphere (711)

1. Introduction

The solar wind is a turbulent plasma flow where energy is transferred across a vast range of scales. The inertial range is the ensemble of large scales where the cascade of energy is produced by the nonlinear interactions of counterpropagating Alfvén waves (Belcher & Davis 1971). The proportion of Alfvén waves propagating in the anti-sunward (outward) direction can differ from the sunward (inward) propagating ones, with the former being the dominant population. The imbalance between the two populations is known as cross helicity and is equivalent to the correlation between velocity and magnetic field fluctuations.

Such imbalance substantially affects the properties of plasma turbulence in the solar wind (Yokoi & Balarac 2011). Phenomenological models have proposed that high cross helicity inhibits the nonlinear transfer of the energy cascade in the solar wind (Dobrowolny et al. 1980; Lithwick et al. 2007; Podesta 2011). This has been supported by estimations of the energy cascade rate computed from solar wind data. For instance, solar wind intervals with a large cross helicity presented lower energy cascade rate values than those with a small cross helicity (Marino et al. 2012). Nevertheless, the transfer of energy from fluctuations in imbalanced solar wind streams provides enough energy to dissipative scales to fulfill the heating required by the solar wind proton temperature evolution (Stawarz et al. 2009; Montagud-Camps et al. 2020).

The aforementioned measurements of low cascade rate in solar winds with large cross helicity are not localized in a particular range of scales. Cross helicity, like energy, is an ideal statistical invariant of the incompressible magnetohydrodynamic (MHD) equations that also cascade to smaller scales at a constant rate over an inertial range. Thus, the study of the cross-helicity turbulence by measuring its cascade rate can bring complementary information on the energy cascade in imbalanced solar winds.

The energy cascade rate can be estimated using phenomenological arguments (Vasquez et al. 2007; Zank et al. 2017). However, methods that compute the temporal evolution of second-order structure functions allow it to be estimated with the least number of assumptions on the basic equations describing the plasma dynamics. First developed for incompressible hydrodynamics (de Karman & Howarth 1938; Monin & Iaglom 1971), the Karman–Howarth–Monin (hereafter KHM) equations were then extended to incompressible MHD (Politano & Pouquet 1998, hereafter PP98; Banerjee & Galtier 2017), allowing also for the cascade rate of cross helicity and the energy of the two Alfvén wave populations, known as pseudo-energies, to be computed separately. In the following years, the anisotropy of the energy cascade in plasmas with a background magnetic field was also taken into account, allowing it to be quantified in solar wind observations and numerical simulations (MacBride et al. 2008; Verdini et al. 2015).

The PP98 equations are still widely used to measure the energy cascade rate in the heliosphere. The solar wind, however, is a medium where compressibility can be non-negligible (Hadid et al. 2017), especially at short heliospheric distances (Shi et al. 2021). This motivated the development of equations to compute the energy cascade rate in plasmas

described with the compressible MHD (CMHD) equations (Banerjee & Galtier 2013; Andrés & Sahraoui 2017; Hellinger et al. 2021).

The existence of slow winds in the vicinity of coronal holes with compressible fluctuations and large cross-helicity values (D'Amicis & Bruno 2015) led us to extend the KHM equation of cross helicity to compressible MHD.

In this work, the new KHM equation for cross helicity is validated with the data of three-dimensional (3D) CMHD numerical simulations. In addition to cross helicity, the KHM equations for energy and pseudo-energies are also used to study several properties of the turbulence developed in our simulations, such as spectral anisotropy and directionality of the cascades.

This paper is structured as follows: In Section 2 we present the KHM equations of CMHD for energy and cross helicity, as well as the KHM equations of the pseudo-energies. In Section 3 we describe our numerical setup, in Section 4 we present the results of the simulations and the KHM analysis performed on them, and Section 5 contains the discussion and main conclusions.

2. Theory

2.1. Karman–Howarth–Monin Equations

In this section, the KHM equations for energy and cross helicity are derived from the CMHD equations,

$$\partial_t \rho + (\boldsymbol{u}\cdot\nabla)\rho + \rho\nabla\cdot\boldsymbol{u} = 0 \tag{1}$$

$$\partial_t \boldsymbol{u} + (\boldsymbol{u}\cdot\nabla)\boldsymbol{u} + \frac{1}{\rho}[\nabla P_t - \boldsymbol{B}\cdot\nabla\boldsymbol{B}] = \frac{\nabla\cdot\boldsymbol{\tau}}{\rho} \tag{2}$$

$$\partial_t \boldsymbol{B} + (\boldsymbol{u}\cdot\nabla)\boldsymbol{B} - \boldsymbol{B}\cdot\nabla\boldsymbol{u} + \boldsymbol{B}\nabla\cdot\boldsymbol{u} = \eta\Delta\boldsymbol{B} \tag{3}$$

$$\partial_t P + (\boldsymbol{u}\cdot\nabla)P + \frac{5}{3}P\nabla\cdot\boldsymbol{u} = \rho\kappa\Delta T + \frac{2}{3}\rho\mathcal{Q}. \tag{4}$$

Quantities in the above equations are normalized with respect to a characteristic length, time, velocity, density, and magnetic field $\mathcal{L} = L_0/(2\pi)$, $\mathcal{T} = t^0_{\rm NL} = L_0/(2\pi u^0_{\rm rms})$, $\mathcal{U} = u^0_{\rm rms}$, $\rho = \rho^0_{\rm rms}$, and $\mathcal{B} = u^0_{\rm rms}\sqrt{4\pi\rho^0_{\rm rms}}$, where the superscript 0 denotes the value of the quantity at the initial time and the subscript rms denotes the rms of the quantity.

In Equation (2), the viscous stress tensor is $\tau_{ij} = \mu(\partial_j u_i + \partial_i u_j - (2/3)\delta_{ij}\partial_k u_k)$, the total pressure is $P_t = P + B^2/2$ and $P = \rho T$ is the plasma thermal pressure. In Equation (4), the turbulent heating per unit volume is $\mathcal{Q} \equiv \left(\boldsymbol{w}\cdot\frac{\nabla\cdot\boldsymbol{\tau}}{\sqrt{\rho}} + \eta|\boldsymbol{J}|^2\right)$, where $\boldsymbol{w} = \sqrt{\rho}\boldsymbol{u}$ is the density-weighted velocity (Kida & Orszag 1990), $\boldsymbol{J} = \nabla\times\boldsymbol{B}$ is the current density, and μ, η, and κ are respectively the dynamic viscosity, resistivity and thermal conductivity.

One of the aims of this work is to assess the influence of thermal compressibility in the cross-helicity cascade. Cross helicity is not an ideal statistical invariant in CMHD, that is, it is no longer conserved when dissipation processes are negligible. Nonetheless, a conservation law can be obtained from Equations (1)–(4),

$$\frac{\partial\langle\boldsymbol{u}\cdot\boldsymbol{B}\rangle}{\partial t} = \left\langle P\nabla\cdot\left(\frac{\boldsymbol{B}}{\rho}\right)\right\rangle - Q_H, \tag{5}$$

where $\langle ...\rangle$ denotes the volume averaging, and the dissipative rate for cross helicity is $Q_H \equiv \left\langle\left(\boldsymbol{B}\cdot\frac{\nabla\cdot\boldsymbol{\tau}}{\rho} + \eta(\boldsymbol{\omega}\cdot\boldsymbol{J})\right)\right\rangle$. The first term on the right-hand side of Equation (5) is the average pressure–dilatation term and allows us to measure the departure of cross helicity from an ideal conservation law. The same apply to the conservation of free energy in CMHD, which takes the form

$$\frac{\partial\langle\boldsymbol{w}^2 + \boldsymbol{B}^2\rangle}{\partial t} = \langle P\nabla\cdot\boldsymbol{u}\rangle - Q_E, \tag{6}$$

where $Q_E = \langle\mathcal{Q}\rangle$.

Even when the pressure–dilatation terms are nonnegligible, the KHM equations can still be derived from the evolution of second-order structure functions. These are computed as $S_2 \equiv \langle\delta\boldsymbol{a}\cdot\delta\boldsymbol{b}\rangle$, where $\delta\boldsymbol{a}$, defined as $\delta\boldsymbol{a}(\boldsymbol{\ell}) \equiv \boldsymbol{a}(\boldsymbol{x}') - \boldsymbol{a}(\boldsymbol{x}) = \boldsymbol{a}' - \boldsymbol{a}$, denotes the spatial increment of the vector field $\boldsymbol{a}$ between pairs of points $\boldsymbol{x}$ and $\boldsymbol{x}' = \boldsymbol{\ell} + \boldsymbol{x}$.

It is common to express the KHM equations in such a way that the nonlinear transfer takes the form of a flux of third-order structure functions. Following the same procedure used in Hellinger et al. (2021) to obtain the KHM equation of energy for compressible Hall MHD, we derived the expression for the nonlinear transfer of cross helicity for CMHD:

$$K_H = -\frac{1}{4}\nabla_\ell\cdot\left\langle\left[\delta\boldsymbol{u}(\delta\boldsymbol{u}\cdot\delta\boldsymbol{B}) - \delta\boldsymbol{B}\frac{1}{2}|\delta\boldsymbol{u}|^2\right]\right\rangle - \left\langle\delta\boldsymbol{B}\cdot\delta\left(\frac{\boldsymbol{J}}{\rho}\times\boldsymbol{B}\right) + (\nabla'\cdot\boldsymbol{u}')(\delta\boldsymbol{u}\cdot\boldsymbol{B}) - (\nabla\cdot\boldsymbol{u})(\delta\boldsymbol{u}\cdot\boldsymbol{B}')\right\rangle, \tag{7}$$

where $\nabla' = \nabla_{x'}$ and $\nabla = \nabla_x$.

The first term on the right-hand side of Equation (7) allows us to measure part of the contribution of incompressible fluctuations to the cross-helicity cascade rate from solar wind observations, provided some assumption on turbulence anisotropy is made. However, measuring the flux of third-order structure functions in numerical simulations is highly computationally demanding. The calculation of spatial increments between every pair $(\boldsymbol{x}, \boldsymbol{x}')$ in three-dimensional simulations requires N^6 operations, with N the number of grid points in one direction.

A way to substantially reduce the computational cost of this process consists on using the cross-correlation property of the Fourier transform on the right-hand side of the following identity

$$\langle\delta\boldsymbol{a}\cdot\delta\boldsymbol{b}\rangle = 2\langle\boldsymbol{a}\cdot\boldsymbol{b}\rangle - \langle\boldsymbol{a}'\cdot\boldsymbol{b} + \boldsymbol{a}\cdot\boldsymbol{b}'\rangle, \tag{8}$$

leading to

$$\langle\delta\boldsymbol{a}\cdot\delta\boldsymbol{b}\rangle = 2\langle\boldsymbol{a}\cdot\boldsymbol{b}\rangle - \mathscr{F}^{-1}(\hat{\boldsymbol{a}}^*\cdot\hat{\boldsymbol{b}} + \hat{\boldsymbol{a}}\cdot\hat{\boldsymbol{b}}^*), \tag{9}$$

where $\mathscr{F}^{-1}(\cdots)$ denotes the inverse Fourier transform, $\hat{\boldsymbol{a}} = \int_{\boldsymbol{x}}\boldsymbol{a}\cdot e^{(i\boldsymbol{k}\cdot\boldsymbol{x})}$ is the direct Fourier transform, and $\hat{\boldsymbol{a}}^*$ denotes the complex conjugate of $\hat{\boldsymbol{a}}$.

In this way, the number of operations is reduced to that of a fast Fourier transform, $(N\cdot\log(N))^3$. In order to take advantage of this improvement in computational efficiency, we used Equation (9) to derive alternative versions of the KHM equations of energy and cross helicity for CMHD and for the pseudo-energies in incompressible MHD.

2.1.1. Energy and Cross Helicity

From Equations (1)–(3), the KHM equations for energy and cross helicity can be obtained using identity (9) and read

$$-\frac{1}{4}\frac{\partial \mathcal{S}_i}{\partial t} + K_i + \Phi_i - D_i = 0, \tag{10}$$

where the subscript $i = E$ corresponds to energy and $i = H$ to cross helicity. The temporal decay KHM terms are defined as

$$\mathcal{S}_E(\ell) = \frac{1}{2}\langle |\delta \boldsymbol{w}|^2 + |\delta \boldsymbol{B}|^2 \rangle \tag{11}$$

$$\mathcal{S}_H(\ell) = \langle \delta \boldsymbol{u} \cdot \delta \boldsymbol{B} \rangle. \tag{12}$$

The temporal variation of these terms in Equation (10) is computed using a forward finite difference method with a time shift of $\Delta t = 10^{-2} t^0_{\rm NL}$. For the other terms, we take the average value between the two times.

The nonlinear transfer terms of Equation (10) read

$$\begin{aligned} K_E(\ell) = -\frac{1}{4}\langle \delta \boldsymbol{w} \cdot \delta[(\boldsymbol{u}\cdot\nabla)\boldsymbol{w} + \frac{1}{2}\boldsymbol{w}\cdot\nabla\cdot\boldsymbol{u}] \\ - \delta\boldsymbol{w}\cdot\delta(\rho^{-1/2}(\nabla\times\boldsymbol{B})\times\boldsymbol{B}) \\ - \delta\boldsymbol{B}\cdot\delta(\nabla\times(\boldsymbol{u}\times\boldsymbol{B}))\rangle \end{aligned} \tag{13}$$

$$\begin{aligned} K_H(\ell) = -\frac{1}{4}\langle \delta\boldsymbol{B}\cdot\delta((\boldsymbol{u}\cdot\nabla)\boldsymbol{u}) - \delta\boldsymbol{B}\cdot\delta(\rho^{-1}(\nabla\times\boldsymbol{B})\times\boldsymbol{B}) \\ - \delta\boldsymbol{u}\cdot\delta(\nabla\times(\boldsymbol{u}\times\boldsymbol{B}))\rangle. \end{aligned} \tag{14}$$

The compressible terms associated to pressure–dilatation effects are

$$\Phi_E(\ell) = -\frac{1}{4}\langle \delta\boldsymbol{w}\cdot\delta(\rho^{-1/2}\nabla P)\rangle \tag{15}$$

$$\Phi_H(\ell) = -\frac{1}{4}\langle \delta\boldsymbol{B}\cdot\delta(\rho^{-1}\nabla P)\rangle, \tag{16}$$

and the terms containing dissipative effects are

$$D_E(\ell) = -\frac{1}{4}\langle \delta\boldsymbol{w}\cdot\delta(\rho^{-1/2}\nabla\cdot\boldsymbol{\tau}) + \eta\delta\boldsymbol{B}\cdot\delta(\Delta\boldsymbol{B})\rangle \tag{17}$$

$$D_H(\ell) = -\frac{1}{4}\langle \delta\boldsymbol{B}\cdot\delta(\rho^{-1}\nabla\cdot\boldsymbol{\tau}) + \eta\delta\boldsymbol{u}\cdot\delta(\Delta\boldsymbol{B})\rangle. \tag{18}$$

We remark that the D_i terms tend to the turbulent heatings Q_i at the largest separation scale. That is, $D_i - Q_i$ represents the effect of the dissipative mechanisms in the system. However, in order to see more clearly the contributions of each term in Equation (10), we do not subtract the total heatings from D_i. In addition, we simply name D_i as dissipative terms, despite being an abuse of language.

2.1.2. Pseudo-energies

Using again Equations (2) and (3) and assuming incompressibility, one can write the equations for the Elsässer fields $z^{\pm} = \boldsymbol{u} \pm \boldsymbol{B}/\sqrt{\rho^0_{\rm rms}}$ as follows

$$\begin{aligned} \partial_t z^{\pm} + (z^{\mp}\cdot\nabla)z^{\pm} + \nabla\left(P + \frac{B^2}{2}\right) \\ = \frac{(\mu\pm\eta)}{2}\Delta z^{+} + \frac{(\mu\mp\eta)}{2}\Delta z^{-}. \end{aligned} \tag{19}$$

The third term on the left-hand side does not contribute to the KHM equations if local homogeneity is also assumed (Carbone et al. 2009). Under these conditions, the pressure–dilatation terms can be omitted from the KHM equations of the pseudo-energies:

$$-\frac{1}{4}\frac{\partial \mathcal{S}_{\pm}}{\partial_t} + K_{\pm} - D_{\pm}, \tag{20}$$

where the temporal decay terms are

$$\mathcal{S}_{\pm}(\ell) = \left\langle \frac{(\delta z^{\pm})^2}{2} \right\rangle, \tag{21}$$

the nonlinear transfer terms read

$$K_{\pm}(\ell) = -\frac{1}{4}\langle \delta z^{\pm}\cdot\delta[(z^{\mp}\cdot\nabla)z^{\pm}]\rangle, \tag{22}$$

and the dissipative terms are

$$\begin{aligned} D_{\pm}(\ell) = -\frac{1}{4}\left\langle \frac{(\mu\pm\eta)}{2}\delta z^{+}\cdot\delta[\Delta z^{+}] \right. \\ \left. + \frac{(\mu\mp\eta)}{2}\delta z^{-}\cdot\delta[\Delta z^{-}].\right\rangle \end{aligned} \tag{23}$$

From Equations (21) to (23), it is possible to compute the KHM terms for energy in incompressible MHD as

$$\mathcal{S}_{zE} = \frac{\mathcal{S}_{+} + \mathcal{S}_{-}}{2},\ K_{zE} = \frac{K_{+} + K_{-}}{2},\ D_{zE} = \frac{D_{+} + D_{-}}{2} \tag{24}$$

and for cross helicity

$$\mathcal{S}_{zH} = \frac{\mathcal{S}_{+} - \mathcal{S}_{-}}{2},\ K_{zH} = \frac{K_{+} - K_{-}}{2},\ D_{zH} = \frac{D_{+} - D_{-}}{2}, \tag{25}$$

where we have denoted incompressible energy and cross helicity as $zE = E^{+} + E^{-}$ and $zH = E^{+} - E^{-}$, respectively.

3. Numerical Setup

The 3D CMHD equations have been solved using a pseudo-spectral method to compute spatial gradients and a Runge–Kutta order three scheme for the evolution in time (Wray 1990). The numerical domain is a box with edge length $2\pi\mathcal{L}$, periodic boundary conditions, and a uniform mesh of 512 grid points in each direction.

Two numerical simulations are analyzed in this work: one without a mean magnetic field, run A, and one with an ambient magnetic field $\boldsymbol{B_0} = (4, 0, 0)b^0_{\rm rms}$, run B. Velocity and magnetic fluctuations have been excited with random phases in all directions for run A and in the planes perpendicular to the ambient magnetic field for run B. For both runs, magnetic and velocity fluctuation amplitudes are initially equal, $u^0_{\rm rms} \sim b^0_{\rm rms} \sim 1$, the initial normalized cross helicity is $\sigma_c = \boldsymbol{u}\cdot\boldsymbol{B}/(u^2 + B^2) = 0.8$, and the initial turbulent Mach number is $M = u_{\rm rms}/c_s = 0.85$ with $c_s = \sqrt{(5/3)T}$. The isotropic magnetic and kinetic energy spectra have a flat initial slope, excited up to a cutoff wavenumber $k_{\rm max} = 4$ for both runs. All other fluctuations have zero amplitude at the beginning of the simulation. No forcing is applied to any fluctuations.

Dynamic viscosity, resistivity, and thermal conductivity have been chosen in order to avoid the accumulation of energy at mesh-size scales and, at the same time, maximize the kinetic and magnetic Reynolds numbers. In order to simplify the selection of the optimal values, we have imposed $\mu = \eta = \kappa$. For run A, $\mu, \eta, \kappa = 1.5\cdot10^{-3}$ and for run B, $\mu, \eta, \kappa = 8\cdot10^{-4}$.

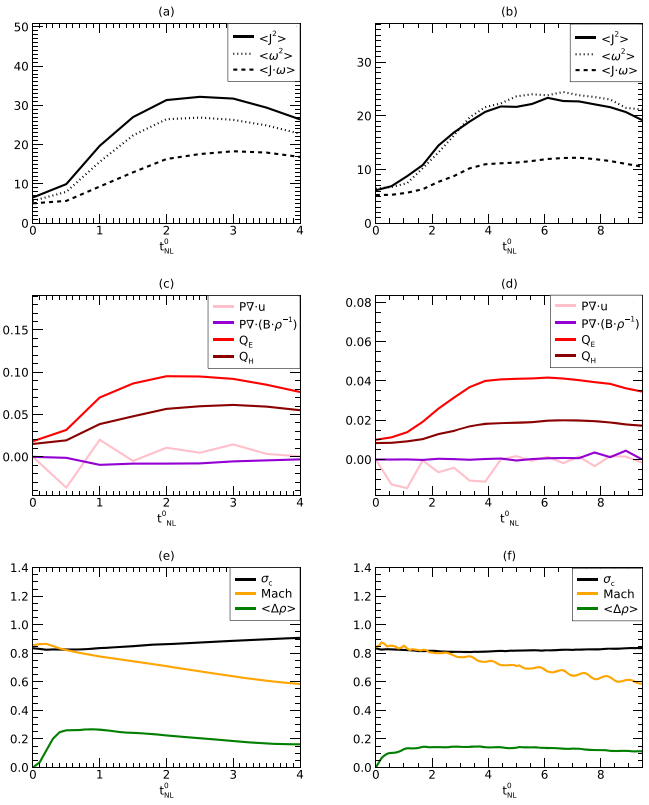

Figure 1. Panels (a), (c), and (e) correspond to run A and panels (b), (d), and (f) to run B. (a) and (b): Temporal evolution of the volume average current density squared $\langle J^2 \rangle$ (solid lines), vorticity $\langle \omega^2 \rangle$ (dotted lines), and cross-current $\langle \boldsymbol{J} \cdot \boldsymbol{\omega} \rangle$ (dashed lines). (c) and (d): Temporal evolution of the averaged pressure–dilatation term for energy $\langle P \nabla \cdot u \rangle$ (magenta lines) and cross helicity $\langle P \nabla \cdot \left(\frac{\boldsymbol{B}}{\rho} \right) \rangle$ (purple lines) and for the turbulent heating of energy Q_E (red lines) and cross helicity (brown lines). (e) and (f): Temporal evolution of normalized cross helicity σ_c (black line), turbulent Mach number (yellow line), and rms of density fluctuations (green line).

4. Results

4.1. Turbulence Properties

In this section, we present the temporal evolution of several relevant plasma parameters, as well as the isotropic spectra after the onset of turbulence.

The peak of turbulent activity for the energy cascade in numerical simulations is taken at the moment the dissipation of turbulent fluctuations has reached a maximum that is followed by a period of constant dissipation, an indication that turbulence is fully developed. The impossibility of writing an explicit expression for turbulent heating in certain numerical simulations leads to the use of other ways to estimate the peak of turbulent activity, such as the measure of the volume average of squared current density, $\langle J^2 \rangle$, or the vorticity, $\langle \omega^2 \rangle$, both included in our expression of the energy heating rate Q_E.

The maximum of $\langle J^2 \rangle$ is, approximately, at 2.5 $t^0_{\rm NL}$ for run A and at 6 $t^0_{\rm NL}$ for run B, as shown in Figures 1(a) and Figure 1(b), respectively. The same figures shows also that the peaks of vorticity, $\langle \omega^2 \rangle$, happen at 2 $t^0_{\rm NL}$ and 6 $t^0_{\rm NL}$ for runs A and B respectively.

The peak of turbulent activity for the cross-helicity cascade can be considered as the maximum of $\langle \boldsymbol{J} \cdot \boldsymbol{\omega} \rangle$, which plays a role in cross-helicity turbulent heating, Q_H, equivalent to the one played by $\langle J^2 \rangle$ for Q_E. The peaks of $\langle \boldsymbol{J} \cdot \boldsymbol{\omega} \rangle$ occur at later

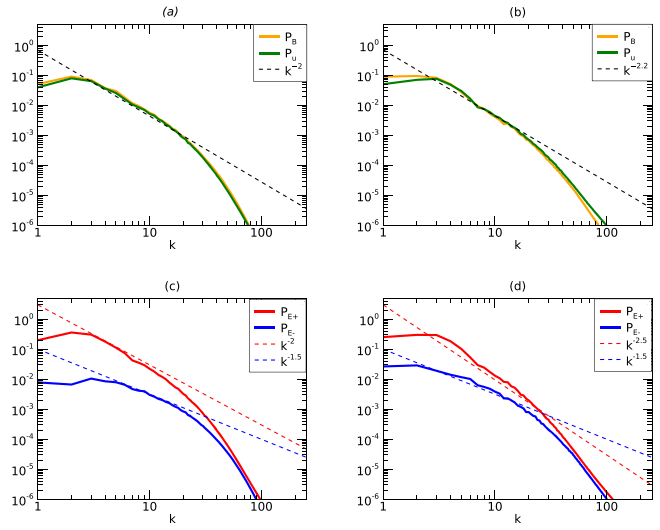

Figure 2. Top row: isotropized spectra of magnetic (orange lines) and velocity fluctuations (green lines) for run A at $t = 3t^0_{\rm NL}$(figure (a)) and run B at $t = 7t^0_{\rm NL}$ (figure (b)). Bottom row: spectra of the pseudo- energies E^+ (red lines) and E^- (blue lines) for run A at $t = 3t^0_{\rm NL}$ (figure (c)) and run B at $t = 7t^0_{\rm NL}$ (figure (d)).

times than for $\langle J^2 \rangle$ and $\langle \omega^2 \rangle$: 3 $t^0_{\rm NL}$ for run A and 7 $t^0_{\rm NL}$ for run B.

Figures 1(c) and (d) show the temporal evolution of the average pressure–dilatation $\langle P \nabla \cdot \boldsymbol{u} \rangle$ and $\langle P \nabla \cdot (\boldsymbol{B}/\rho) \rangle$ and the heating rates for energy and cross helicity Q_E and Q_H, for runs A and B, respectively.

The maximum of cross-helicity heating takes place in both runs at the same time that $\langle \boldsymbol{J} \cdot \boldsymbol{\omega} \rangle$ peaks in Figures 1(a) and (b), therefore indicating the importance of $\langle \boldsymbol{J} \cdot \boldsymbol{\omega} \rangle$ structures in the dissipation of cross helicity. The maxima of Q_E are reached at the same time as $\langle \omega^2 \rangle$.

The average pressure–dilatation decreases substantially after the peaks of Q_E. From that moment onwards, the average pressure–dilatation terms remain at least one order of magnitude smaller than the heating rates for run A. For run B, the ratio between average pressure–dilatation terms and Q_E and Q_H are even smaller. In other words, the development of turbulence and the presence of a background mean magnetic field substantially reduces the pressure–dilatation term in the conservation Equations (6) and (5) and therefore $\boldsymbol{u} \cdot \boldsymbol{B}$ and $\boldsymbol{w}^2 + \boldsymbol{B}^2$ become closer to ideal statistical invariants of CMHD.

The small amplitudes for the pressure–dilatations are obtained under relatively high turbulent Mach number, $M = u_{\rm rms}/c_s$ with $c_s = \sqrt{(5/3)T}$, which decreases from 0.8 to 0.6 in both runs (Figure 1(e) for run A and Figure 1(f) for run B). The same panels show how, during a short period of relaxation for the initial conditions, there is a short increase of density fluctuations $\Delta\rho = \langle \langle \rho \rangle - \rho \rangle$. After reaching its maximum around $0.2\rho^0_{\rm rms}$, it decrease monotonically. Conversely, the normalized cross helicity, $\sigma_c = \boldsymbol{u} \cdot \boldsymbol{B}/(\boldsymbol{u}^2 + \boldsymbol{B}^2)$, increases with time after the relaxation period of the initial conditions, as is characteristic of numerical simulations without expansion of the plasma (Grappin et al. 1982, 2016). The presence of the mean magnetic field in run B slows down the temporal evolution of these plasma parameters but maintains their overall behavior.

Figures 2 (a) and (b) show respectively the spectra of magnetic and kinetic fluctuations computed at the peaks of cross-helicity turbulence: at $3t^0_{\rm NL}$ for run A and at $7t^0_{\rm NL}$ for run

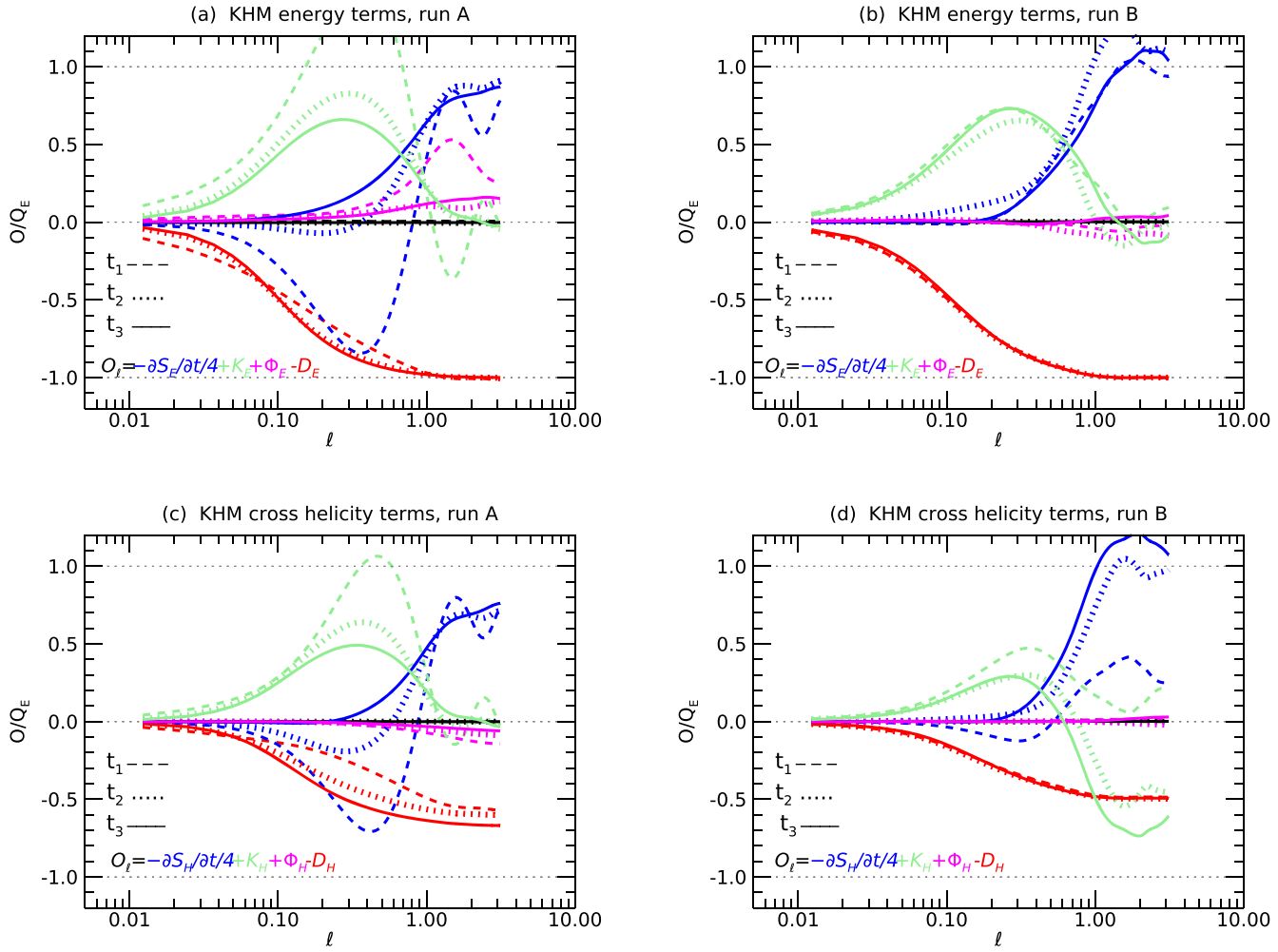

Figure 3. Temporal evolution of the KHM terms of energy and cross helicity for runs A and B. The KHM terms have been computed at $t_1 = 1t^0_{\rm NL}$, $t_2 = 2t^0_{\rm NL}$ and $t_3 = 3t^0_{\rm NL}$ for run A and at $t_1 = 6t^0_{\rm NL}$, $t_2 = 7t_{\rm NL}$ and $t_3 = 8t_{\rm NL}$ for run B. The validity tests $\mathcal{O}_\ell$ are represented by black lines. The other lines correspond to the dissipative terms D_i (red lines), the temporal decay $\partial S_i/\partial t/4$ (blue lines), the nonlinear transfer rate term K_i (green lines), and the pressure–dilatation term Φ_i (magenta lines), where the subscript $i = E$ denotes the energy KHM terms and $i = H$ the cross-helicity ones.

B. In Figure 2(a), magnetic and kinetic fluctuations have an isotropic spectra with a slope of -2. In Figure 2(b), the slopes are slightly steeper, proportional to $k^{-2.2}$. These spectral indices are steeper than the $-5/3$ of Kolmogorov's prediction (Kolmogorov 1941) or the $-3/2$ of the Irishnikov-Kraichnan phenomenology (Iroshnikov 1963; Kraichnan 1965), being closer to the -2 predicted for weak MHD turbulence (Galtier et al. 2000) or the -2 predicted by Burger for shock-based turbulence phenomenology (Frisch 1995). The former two phenomenologies are unlikely to explain the observed spectra in our simulations. Weak turbulence takes place when magnetic fluctuations are at least an order of magnitude smaller than the mean field (Meyrand et al. 2015) and this phenomenology would not be able to explain the -2 index in the run with no background magnetic field. On the other hand, Burger's phenomenology can also be discarded owing to the fact that both runs were initialized with subsonic fluctuations and no substantial amount of shocks can be developed in a pseudo-spectral code, such as the one we are using.

The spectral indices in our simulations respond instead to the inefficiency of nonlinear interactions in producing an effective energy transfer, caused by the initial imbalance of the Alfvénic populations and the difficulty of achieving higher Reynolds numbers. The inefficiency of the cascade is further commented on in Section 4.2.

The kinetic and magnetic spectra are almost superposed in both cases, except for $k < 2$, where there is a small magnetic excess for both runs. The spectra of the pseudo-energies $E^+ = |\boldsymbol{z}^+|^2/2$ and $E^- = |\boldsymbol{z}^-|^2/2$ are computed at the same time as the velocity and the magnetic spectra and are shown in Figure 2(c) for run A and Figure 2(d) for run B. Both runs show dominance of the $\boldsymbol{z}^+$ Alfvén wave energy over that of $\boldsymbol{z}^-$, with the spectra of the former steeper than the latter. In the solar wind, these spectra remain almost parallel at inertial range scales (Chen et al. 2020). Conversely, the pinning of the Elsässer spectra is characteristic of simulations that do not account for expansion of the solar wind in the directions transverse to the heliospheric radial (Verdini et al. 2019).

4.2. Energy and Cross-helicity Cascades in Compressible MHD

Figure 3 shows the KHM terms of energy and cross helicity isotropized in separation space, so they only depend on the modulus of ℓ.

We have selected three times to show the temporal evolution of the KHM terms for energy and cross helicity close to their

respective peaks of turbulent activity. For run A, $t_1 = 1t^0_{\rm NL}$ corresponds to one turnover time prior to the peak of the energy heating rate, which occurs at $t_2 = 2t^0_{\rm NL}$. Finally, $t_3 = 3t^0_{\rm NL}$ is taken at the peak of the cross-helicity heating rate.

Conversely, for run B, the first time is the maximum energy heating rate, $t_1 = 6t^0_{\rm NL}$, and $t_2 = 7t^0_{\rm NL}$ is the peak of Q_H. As will be further explained later in this section, the temporal decay term of energy grows in the inertial range at $7t^0_{\rm NL}$ and becomes nonnegligible. In order to discard our conclusions that the energy and cross-helicity cascades of run B could be attributed to a short-lived phenomenon, we chose $t_3 = 8t^0_{\rm NL}$, when the temporal decay term is again negligible within the inertial range.

The KHM terms at time t_1 in Figures 3(a)–(d) are represented with dashed lines, t_2 with dotted lines, and t_3 with solid lines. All KHM terms are normalized to the energy heating rate, Q_E, of their respective run and time. This normalization allows for an easy comparison of the efficiency of the nonlinear transfer of the energy and the cross-helicity cascades.

The KHM terms of energy and cross helicity fulfill Equation (10) for all three times in run A, with errors (black lines) smaller than $1\%Q_E$. The presence of a mean magnetic field in run B is not reflected on the error $\mathcal{O}_\ell$, which also remains below $1\%Q_E$ at all times.

The time delay between the peaks of Q_E and Q_H for run A observed in Figure 1(c) can be seen in terms of the evolution of the temporal decay terms (blue lines) in Figures 3(a) and 3(c). During the onset of the cascades, the decay terms of energy and cross helicity present negative values at intermediate scales. At the peak of Q_E, the energy decay terms are already close to zero for $\ell < 0.5$ while this does not happen to the temporal decay terms of cross helicity until the peak of Q_H.

In Figure 3(b), the temporal decay terms of the energy cascade for run B is close to zero for scales $\ell < 0.5$ at $t_1 = 6t^0_{\rm NL}$. As for run A, cross-helicity decay terms will not reach this situation until the peak of Q_H at $t_2 = 7t^0_{\rm NL}$ (Figure 3(d)). Thus, the KHM analysis also confirms that the slower development of the cross-helicity cascade is not affected by the presence of a background magnetic field.

We remark that for run B, there is a nonnegligible increase of the temporal decay term of energy at $t_2 = 7t^0_{\rm NL}$ for all scales (see Figure 3 (b)). This increase is only temporary and the decay term decreases back to its previous state after a turnover time, at $t_3 = 8t^0_{\rm NL}$. This fluctuation of the decay term also alters the nonlinear transfer of energy (green lines).

In the absence of the KHM analysis, one could assume that at $t_2 = 7t^0_{\rm NL}$ the turbulence is already well developed based on the temporal evolution of Q_E or $\langle J^2 \rangle$, leading to conclusions on the energy cascade rate that could not be valid after a nonlinear time. Thus, even though the dissipation rates Q_E and Q_H (or $\langle J^2 \rangle$ and $\langle \boldsymbol{J} \cdot \boldsymbol{\omega} \rangle$ in the absence of an explicit expression for the heating) can be considered as good proxies to establish the maximum of turbulence activity, the KHM analysis provides a more accurate description of the turbulence properties at all scales, allowing transitory changes of the cascades to be detected that would be unnoticed otherwise.

The KHM dissipative terms, $-D_E$ and $-D_H$, also display the slower development of the cross-helicity cascade, although less clearly than the temporal decay terms. Figure 3(a) shows that the energy dissipation terms already converge after t_2 while the cross-helicity dissipative terms in Figure 3(c) still show some differences between times t_2 and t_3. Conversely, for run B, the dissipation terms of energy and cross helicity in Figure 3(b) and Figure 3(d) are almost completely superposed for all three times. Thus, the dissipative process seems to be more stable in the presence of the mean magnetic field. This is compatible with the small temporal variations of the heating rates Q_E and Q_H in Figure 1(d) once their respective maxima have been reached. Taking into consideration that the magnetic reconnection rate in Hall MHD simulations is reduced by strong guide fields (Pritchett & Coroniti 2004; Huba 2005; Tharp et al. 2013; Widmer et al. 2016), the stability of the dissipative process in run B might also be related to the influence of the mean field on the current sheets and the effect of these structures on the heating process.

The evolution of the flows toward the maxima of turbulence activity does not have any remarkable effect on the KHM pressure–dilatation terms Φ_E and Φ_H, besides a decrease of their amplitude in time. These KHM terms reach their maxima at large scales, generally around $\ell > 1$. The amplitude of Φ_E is larger than Φ_H at all times and for both runs. In Figures 3(a) and 3(c), Φ_H for run A have the opposite sign to Φ_E, but this does not happen in Figures 3(b) and 3(d) for run B.

In the latter, the pressure–dilatation KHM terms oscillate around zero and their amplitudes are between two and five times smaller than for run A. Thus, the presence of a background magnetic field reduces the pressure–dilatation effects in turbulence and favors the changes of sign of Φ_E and Φ_H. However, the oscillations of the pressure–dilatation term can still be developed even in the absence of the mean field, provided that the simulation is allowed to evolve for a long-enough time. The application of the KHM equation of energy for three-dimensional compressible hydrodynamic simulations proved that the oscillations can also appear in isotropic turbulent flows (Hellinger et al. 2021).

The nonlinear transfer terms K_E and K_H of runs A and B at the peaks of turbulent activity show that the energy and cross-helicity cascade are not efficient enough in our simulations. All nonlinear transfer terms peak at intermediate scales, approximately at $\ell \approx 3$, and do not reach critical heating levels. For the cross-helicity cascade, that level should be reached at $Q_H \approx 0.7Q_E$ for run A and $Q_H \approx 0.5Q_E$ for run B. The range of scales where the K_E and K_H values are close to their maxima is also narrow, not much more than half a decade.

The relatively large turbulent Mach number with which we set up the simulations limited our capacity to achieve higher Reynolds numbers and therefore, contributed to limiting the extension of the inertial ranges and the efficiency of the nonlinear transfers. However, for run B, the isotropization of the KHM terms in Figures 3(b) and 3(d) hides the improvement of the efficiency of the cascades in the directions transverse to the mean magnetic field. This point will be further discussed in Section 4.5.

In spite of the limited efficiency of the cascades, the K_E and K_H show one remarkable trait. For run B, the nonlinear transfers of energy and cross helicity split into two: Scales below $\ell \approx 1$ present positive K_E and K_H values and negative ones for scales above $\ell \approx 1$. After the onset of turbulence, the splitting of the cascades does not take place for run A, signaling the importance of the background magnetic field for this process.

In run A, once the peak of Q_E is reached, K_E and K_H are positive and $K_E \geqslant K_H$ at all scales. The latter means that the

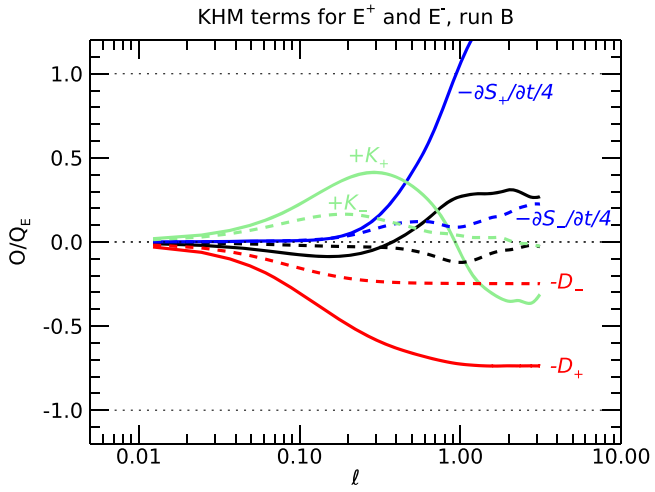

Figure 4. Isotropized KHM terms for the pseudo-energies E^+ (solid lines) and E^- (dashed lines) as a function of separation scale ℓ, computed for run B at time $t = 8t_{\rm NL}^0$, after the peaks of maximum turbulent activity for energy and cross helicity. All terms are normalized to the energy heating rate Q_E. The color code is the same as in Figure 3.

nonlinear transfer of energy is more efficient than that of cross helicity. In the range of scales where the nonlinear transfers are positive for run B, $K_E \geqslant K_H$, too. Conversely, the opposite happens in the range of negative values, where the nonlinear transfer of the cross-helicity cascade is the more efficient of the two. This feature of the nonlinear transfer for run B is not short-lived and remains for several turnover times, until the end of the simulation (not shown).

We will discuss the splitting of the energy and cross-helicity cascades in detail in Section 5.

4.3. Estimation of the Cascade Rate for the Pseudo-energies

The pseudo-energies E^+ and E^- are ideal statistical invariants of the incompressible MHD equations that, like energy and cross helicity, cascade through a range of scales as a result of nonlinear interactions. Assuming that compressible effects are negligible, the incompressible energy and cross helicity can be written in terms of the Elsässer energies as $zE \equiv E^+ + E^-$ and $zH \equiv E^+ - E^-$, respectively. Consequently, the KHM terms of E^+ and E^- allow the nonlinear transfers to be interpreted in terms of the outward and inward Alfvén wave populations.

In this section, we compute the KHM terms of the pseudo-energies as defined in Equations (21)–(23) and use them to study the splitting of the energy and cross-helicity cascades in run B. Figure 4 presents the KHM terms of E^+ and E^- computed at $t = 8$ and normalized to the energy heating rate Q_E.

Since E_+ is the dominant Alfvén wave population, its KHM terms resemble those of the energy cascade in Figure 3(b). However, for scales $\ell > 1$, the negative values of the nonlinear transfer K_+ are closer to the cross-helicity ones in Figure 3(d). But unlike cross helicity, the pseudo-energies are positive definite and therefore the negative values of K_+ imply that an inverse cascade of E^+ is taking place at large scales.

This inverse cascade of E^+ exists even if the error introduced by the assumption of incompressibility is taken into account. Such error is represented by the solid black line in Figure 4. It is concentrated at large scales $\ell > 0.8$, where it reaches about $30\%Q_E$. The positive sign in the error implies that, due to compressibility, the energy transfer rate at large scales could be between the maximum of K_+, $-40\%Q_E$ and, at most, $-70\%Q_E$. The last value is obtained assuming that K_+ is the only KHM term of E^+ affected by compressible effects.

For the subdominant pseudo-energy E^-, the nonlinear transfer term K_- is always positive and therefore corresponds to a direct cascade of E^-. Like before, even if the error associated with the incompressible assumption (dashed black line in Figure 4) is completely assigned to K_-, that would not change the direction of the cascade of E^- toward small scales.

4.4. Effect of Compressibility in the Energy and Cross-helicity Cascade Estimations

In the classic formulation of the KHM equations of energy and cross helicity, the incompressible and compressible contributions to the nonlinear transfers are separated into different terms (see Equation (7)). With the alternative KHM equations we presented in Section 2.1.1, it is not possible to directly isolate the compressible contributions. However, it can be done by comparing the KHM terms for CMHD with the incompressible ones for energy, zE, and cross helicity, zH.

Figures 5(a) and (b) show with dashed lines the KHM terms for energy and cross helicity for CMHD, computed for run B at $t = 8t_{\rm NL}^0$ according to Equations (11)–(18). Conversely, solid lines correspond to the KHM terms for energy and cross helicity computed from the Elsässer fields following Equations (24) and (25).

The comparison in Figure 5(a) between the nonlinear transfer of energy computed from the Elsässer fields, K_{zE}, and the transfer computed from CMHD, K_E, proves that compressibility favors the direct cascade of energy toward small scales. On the one hand, both quantities are positive and peak at $\ell \approx 0.3$, where K_E is approximately $10\%Q_E$ larger than K_{zE}. On the other hand, their minima are reached at $\ell \approx 3$, where both quantities are negative and K_{zE} is almost $20\%Q_E$ smaller than K_E. Therefore, compressibility not only enhances the direct cascade of energy but also contributes to inhibiting its large-scale inverse cascade.

Compressibility plays a more complex role in the cross-helicity turbulent cascade. In Figure 5(b), at scales larger than $\ell \approx 0.3$, K_H is always below K_{zH}. Both transfers are positive for $\ell \lesssim 1$ and change the sign at larger scales. Consequently, above $\ell \approx 0.3$, compressible fluctuations inhibit the positive transfer of cross helicity and enhance the negative one. At scales smaller than $\ell \approx 0.3$ however, K_H is larger than K_{zH}, indicating that compressibility benefits the positive transfer of cross helicity at these scales.

The incompressible version of the KHM terms for energy and cross helicity provides a good approximation, not only of the positive nonlinear transfer but of the other KHM terms, too. For scales below $\ell \approx 0.3$, the nonlinear transfers of energy and cross helicity are positive and are the main contributors to the total error (solid black lines in Figures 5(a) and 5(b)), which does not surpass 10% of the energy and cross-helicity heating rates.

On the contrary, at large scales, where the negative nonlinear transfer takes place for both cascades, the total error of the incompressible KHM equations becomes considerably larger, especially for cross helicity. While for incompressible energy, zE, the total error amounts to $20\%Q_E$, for zH it rises up to $70\%Q_H$. Hence, compressible fluctuations have a greater presence at large scales.

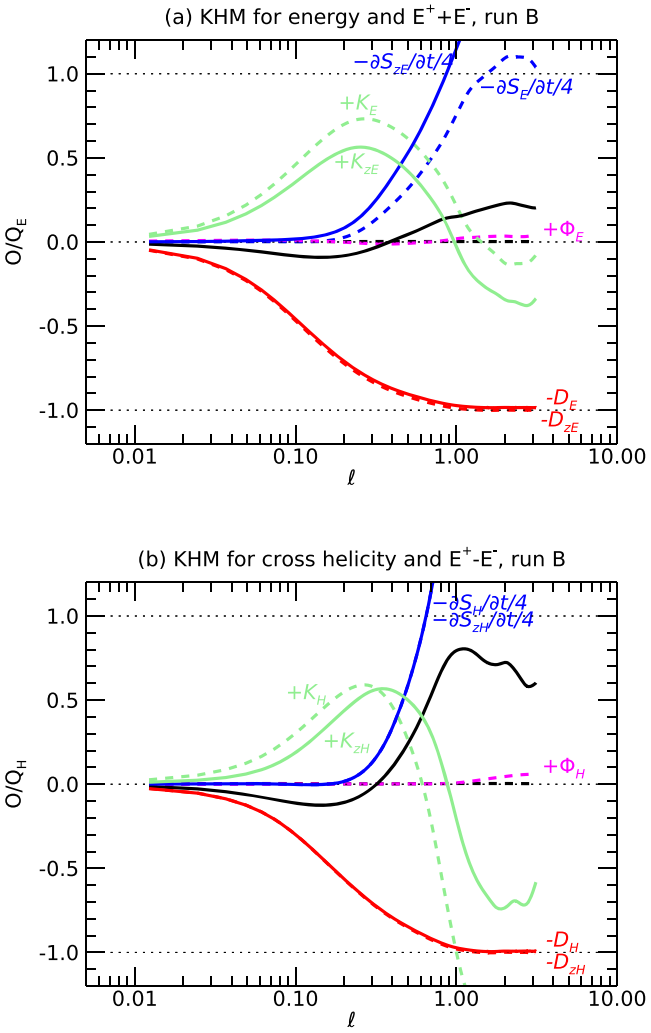

Figure 5. (a) Isotropized KHM terms of energy E (dashed lines) and $zE = E^+ + E^-$ (solid lines) for run B at $t = 8t_{\rm NL}^0$. (b) Isotropized KHM terms of cross helicity H (dashed lines) and $zH = E^+ - E^-$ (solid lines) for run B at $t = 8t_{\rm NL}^0$. The color code is the same as in Figure 3.

4.5. Anisotropy of the Energy and Cross-helicity Cascades

In this section, the anisotropy of the energy and the cross-helicity cascades of run B are analyzed by taking three one-dimensional (1D) cuts of the KHM terms of CMHD before its isotropization. The cuts are taken at $t = 8t_{\rm NL}^0$ in the direction of the mean field, the x-axis ($\theta_B = 0^o$), along the y-axis ($\theta_B = 90^o$), and along the bisector of both axes ($\theta_B = 45^o$).

Panels (a), (b), and (c) of Figure 6 show the anisotropy of the KHM terms for the energy cascade. All KHM terms for energy are normalized to the energy heating rate of the whole numerical domain, Q_E.

In panel (a), the nonlinear transfer is positive along the mean magnetic field direction, although it reaches only moderate values, $20\%Q_E$ for scales $\ell < 0.8$. The dissipative effects are already nonnegligible at those scales. For larger scales, K_E takes large negative values, even below $-1Q_E$. The temporal decay term rises above the Q_E line in order to balance the back transfer of energy.

The pressure–dilatation terms for energy, Φ_E, in Figures 6(a)–6(c) are only nonnegligible at scales larger than $\ell > 0.8$, but even there their absolute value remains below $10\%Q_E$. The sign of Φ_E changes with the inclination θ_B, but unlike the other terms, it does not display any clear anisotropy.

Figures 6(b) and 6(c) show that the nonlinear transfer term for energy increases at all scales when approaching the directions transverse to the mean field. In Figure 6(c), there is a well-developed inertial range within $\ell \in [0.1, 1]$, where the nonlinear term reaches $K_E \approx 80\%Q_E$. In Figure 6(b) we already see large positive values of K_E, but with some fluctuations for $\ell > 0.3$.

In panel (c) of Figure 6, for scales $\ell > 2$ perpendicular to $\boldsymbol{B}_0$, there is an inverse nonlinear transfer, but it only reaches $-40\%Q_E$. This back transfer seems restricted to almost perpendicular scales. Large scales in Figure 6(b) do not show negative values of K_E along $\theta_B = 45^\circ$.

The dissipative terms along 45° and 90° increase for separation scales smaller than 0.2, which is compatible with an energy cascade developed predominantly in directions perpendicular to the ambient magnetic field.

The temporal decay terms anisotropy seems to be adapted to that of the nonlinear transfer terms, so it can maintain Equation (10) valid in all directions.

The cross-helicity turbulence anisotropy is analyzed in panels (d), (e), and (f) of Figure (6). The KHM terms of cross helicity are normalized to Q_H computed on the whole numerical domain.

The anisotropy of the cross-helicity cascade is qualitatively similar to the energy cascade one with regard to the dissipative and the pressure–dilatation terms. The nonlinear transfer term K_H in Figure 6(f) also presents an extended inertial range in the direction perpendicular to B_0, within the scales $\ell \in [0.3, 1]$, where $K_H \approx 70\%Q_H$.

As was already seen when comparing the isotropic KHM terms in Figures 3(b) and 3(d), the negative values of K_H in Figure 6(f) are more than four times greater than for K_E in Figure 6(c) and over a longer range of scales, $\ell > 1$.

However, for the cross-helicity cascade, it is not clear whether this large scales behavior of K_H is only restricted to highly oblique inclinations. In Figure 6(e) one can observe the variations of the nonlinear transfer term, similar to K_E in Figure 6(b), but with a larger amplitude.

In order to have a more complete view of the variations of the nonlinear transfers of energy and cross helicity with the magnetic field inclination, we have gyrotropized the 3D fields, $K_E(\ell)$ and $K_H(\ell)$, about the B_0 axis. Taking into account the results in Figures 6(a)–(f), we use a log–log scale to highlight the nonlinear transfers in the highly oblique and parallel directions, where it is expected that the transfers reach their maxima and minima.

In Figure 7(a), the gyrotropized nonlinear transfer of energy, $K_E(\ell_\parallel, \ell_\perp)$, confirms the preferential development of the direct energy cascade in the directions transverse to the ambient mean field. On the other hand, the inverse energy cascade takes place at large scales, in the quasi-parallel and the quasi-perpendicular directions. Contrary to the direct cascade, the back transfer of energy is dominant in the directions parallel to the mean magnetic field. Furthermore, parallel and perpendicular back transfers are separated by a region of positive K_E. This gap between the two regions with negative K_E values suggests that each of them corresponds to different inverse cascades. An alternative interpretation is that the limited size of the numerical domain suppresses part of the nonlinear interactions

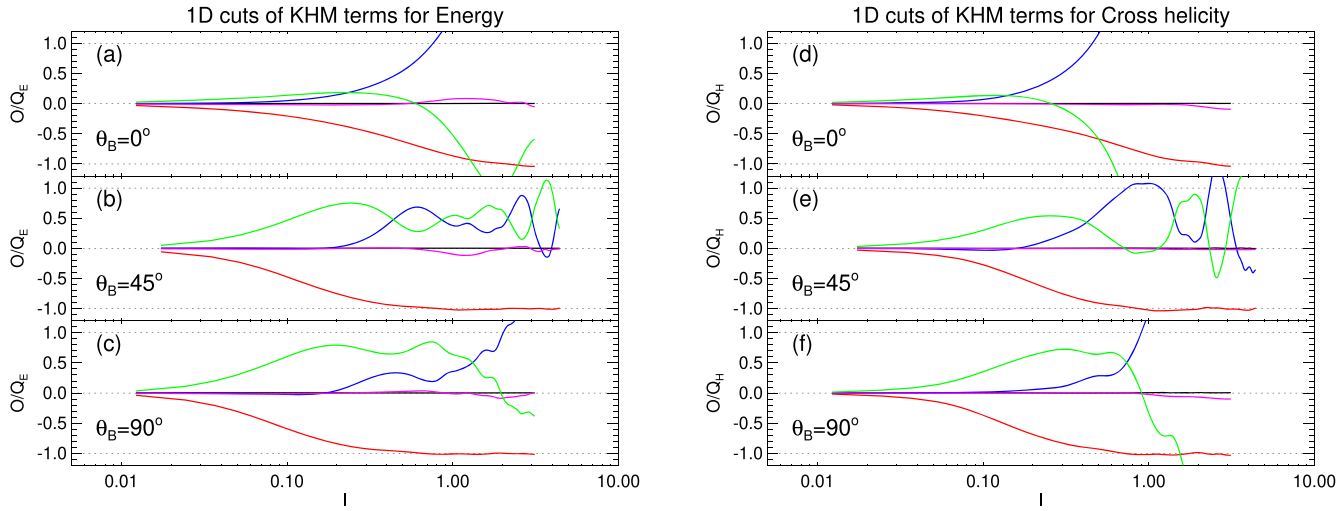

Figure 6. 1D cuts of the KHM terms in the plane xy for run B at $t = 8t_{\rm NL}^0$. The angle θ_B indicates the inclination of the cut with respect to the mean field, with $\theta_B = 0^0$ corresponding to the cut along the mean field axis. Panels (a), (b), and (c) correspond to the KHM terms for energy and panels (d), (e), and (f) to cross helicity. The color code is the same one used in Figure 3.

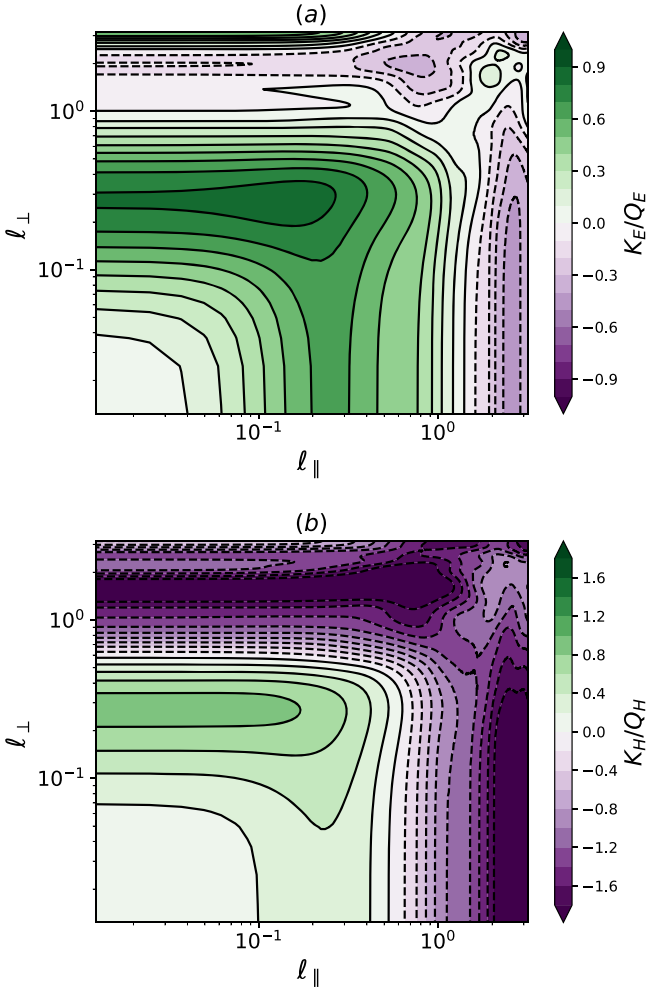

Figure 7. (a) Gyrotropization of $K_E(\ell)/Q_E$ for run B at time $8t_{\rm NL}^0$. (b) Gyrotropization of $K_H(\ell)/Q_H$ for run B at time $8t_{\rm NL}^0$.

in the oblique directions at large scales, thus giving the appearance of two independent inverse cascades.

The gyrotropized nonlinear transfer of cross helicity in Figure 7(b), $K_H(\ell_\parallel, \ell_\perp)$, is qualitatively similar to $K_E(\ell_\parallel, \ell_\perp)$. In both cases, the positive nonlinear transfers reach their maximum values in the directions perpendicular to the mean field and two seemingly independent negative nonlinear transfers are present at large scales. The main difference between the energy and cross-helicity cascades is whether the positive transfers reach larger values than the negative ones. The latter is the case for the energy, while for cross helicity the opposite occurs. Moreover, unlike for the energy inverse cascades, the negative nonlinear transfer of cross helicity in the perpendicular directions reaches similar values to those in the quasi-parallel directions.

The complementarity of the energy and cross-helicity transfers can be explained as a consequence of the coupling between the two cascades. As pointed out in (Andrés et al. 2022), the coupling appears naturally in the classical formulation of the KHM equations. Dimensional analysis of Equation (7) shows that the divergence of the flux of third-order structure functions (the main contributor to the cascade rate) can be written in terms of energy and cross helicity,

$$K_H \approx (u \cdot H - B \cdot E/2)/L, \tag{26}$$

where $H = u \cdot B$ and $E \approx (u^2 + B^2)/2 \approx u^2$. The same can be done for the energy nonlinear transfer using the term $\nabla \cdot \boldsymbol{Y}$ in Equation (4) of Hellinger et al. (2021) and assuming incompressibility,

$$K_E \approx (2u \cdot E - 2B \cdot H)/L. \tag{27}$$

Equations (26) and (27) suggest that an increase of energy would also increase the nonlinear transfer of energy while decreasing that of cross helicity, while the opposite would be true for an increase of cross helicity. However, changes of sign in velocity, magnetic field, or cross helicity can alter this relation and induce further differences, such as the negative nonlinear transfer of cross helicity having similar values in the parallel and perpendicular directions.

5. Discussion

We have used an alternative method to compute the KHM terms for various quantities, namely energy and cross helicity for CMHD and energy, cross helicity, and the pseudo-energies

for incompressible MHD. Instead of expressing the nonlinear transfer as a flux of third-order structure functions (classic KHM, hereafter), we computed all KHM terms as second-order structure functions using Equation (9) (alternative KHM). Both approaches are mathematically consistent and numerically equivalent (not shown), but the alternative approach reduces significantly the numerical cost of computing the KHM terms. It also provides, as a by-product of the calculation, the terms of the spectral transfer equations (Grete et al. 2017; Hellinger et al. 2021) that allow the nonlinear transfers in Fourier space to be computed.

We have made use of the numerical efficiency of the alternative approach to compute all terms of the KHM equations for energy and cross helicity with data from 3D CMHD simulations with high cross helicity. We remark the following results from our analysis of the KHM terms:

1. The onset of the energy cascade takes a shorter time than cross helicity. The time shift is approximately a turnover time and is not affected by the presence of a mean magnetic field. A phenomenological model for the cross-helicity dissipation rate developed in Yokoi (2011) allows the longer onset period for the cross-helicity cascade to be related to their heating rates. According to such a model, the characteristic nonlinear times for energy and cross helicity can be assumed to be

$$\tau_E = C_{E0} Q_E^{-1/3} k^{-2/3} \tag{28}$$

$$\tau_H = C_{H0} Q_H^{-1/3} k^{-2/3}, \tag{29}$$

where C_{E0} and C_{H0} are numerical factors. The inequality $\tau_H > \tau_E$ is fulfilled if $(C_{E0}/C_{H0}) < (Q_H/Q_E)^{-1/3}$. If the numerical constants are equal, that only leaves as a condition the heating rate for energy to be larger than that for cross helicity. The latter is fulfilled for both of our runs, as shown in Figures 1(c) and (d). The similar time shift between the onsets for both runs despite having different ratios Q_H/Q_E suggests that the condition $C_{E0} = C_{H0}$ can be weakened.

The existence of a time shift between the energy and cross-helicity cascades implies that turbulence shall not be considered as fully developed in the system until the slowest cascade has reached stationarity since the properties of the fastest cascade can still be affected by changes in the slower one. This can be of importance for certain phenomena in the heliosphere, particularly in situ ations where high cross-helicity winds interact with low cross-helicity plasmas, such as the magnetosphere. Recently, a causal link has been found between the longer duration of the recovery phase of geomagnetic storms and the arrival of solar wind streams with large cross helicity after the solar drivers of the storms (Telloni et al. 2021). The need for more time for the cross-helicity cascade to fully develop in the magnetosphere could be related to the longer period needed by the magnetosphere to recover its properties prior to the arrival of the solar driver. The KHM equation for cross helicity derived in this work for CMHD could be applied to numerical simulations of the magnetosphere to verify this relation.
2. In presence of a mean magnetic field, the nonlinear transfer of energy and cross helicity splits into a positive transfer at intermediate scales and a negative one at large scales. While energy is positive definite and therefore the sign of the nonlinear transfer determines the direction of the cascade, this correspondence cannot be made to unsigned definite quantities such as cross helicity. The negative nonlinear transfer of cross helicity that we observe in our simulations could correspond to either an inverse cascade of cross helicity or a direct cascade of negative cross helicity.

Since fluctuations are freely decaying in our simulations, it is difficult to identify the generation of large-scale structures in real space that would characterize an inverse cascade. However, the analysis of the KHM terms allows us to discriminate between the inverse cascade of cross helicity and a direct cascade of negative cross helicity at large scales.

On the one hand, a direct transfer of negative cross helicity would change the sign of the other KHM terms and of the cross-helicity heating Q_H. Since the other KHM terms of cross helicity keep their sign when normalized to Q_E, as shown in Figure 3, we can discard the nonlinear transfer of cross-helicity cascades in the same direction at all scales.

On the other hand, the analysis of the KHM terms for the pseudo-energies also supports that the incompressible part of the negative nonlinear transfer of cross helicity at large scales corresponds to an inverse cascade. Like energy, the pseudo-energies are also positive definite quantities and thus the sign of their nonlinear transfer indicates the direction of their cascades. Hence, we identified that at large scales, the initially dominant pseudo-energy E^+ has an inverse cascade while E^- keeps a small direct cascade. In other words, a larger imbalance between both Alfvénic populations is being created at large scales.

Negative values of the nonlinear transfers of the energy and the cross-helicity cascade have been measured in certain solar wind intervals, where positive and negative values of the cascade rates alternate, displaying patchy inertial ranges (Smith et al. 2009, 2018; Stawarz et al. 2010; Coburn et al. 2015; Vasquez et al. 2018). It has been argued that one possible mechanism leading to this phenomenon in the solar wind could be the formation of large-scale 2D layers in a plasma flow with a strong background magnetic field (Sorriso-Valvo et al. 2007). Indeed, the coexistence of direct and inverse energy cascades has been observed to take place when flows suffer some degree of two-dimensionalization, such as turbulence in thin layers (Musacchio & Boffetta 2017; Alexakis & Biferale 2018) or in strongly rotating 3D fluids (Morize et al. 2005; Mininni & Pouquet 2009). In run B, the inverse cascades take place at the injection scales, where the initial fluctuations were not excited in the direction parallel to the mean field. The persistence of such initial 2D large-scale structures, favored by the presence of an intense mean magnetic field, could have triggered the inverse cascades. At the same time, the development of a strong parallel back transfer of cross helicity at large scales may have also contributed to weakening the energy cascade in the parallel direction, where the nonlinear interactions are less efficient, thus acting in the benefit of the two-dimensionalization of the flow. Our results are therefore compatible with the interpretation made in Sorriso-Valvo et al. (2007) about

the origin of the inverse transfer patches in the measurements of the cascade rate. However, further study is needed to determine to what extent the initialization with solenoidal fluctuations, the background magnetic field and cross helicity contribute to the inverse cascades.

3. The comparison between the KHM terms of energy and cross helicity for compressible MHD with their corresponding versions for incompressible MHD has shown that the contribution of the compressible fluctuations to nonlinear transfers depends on the direction of the cascade.

   On the one hand, for the direct cascades of energy and cross helicity, the contribution of compressible fluctuations is small, but not negligible. In our simulations, with a Mach number close to 0.6 at the moment of measuring the KHM terms, the compressible contribution increases the direct nonlinear transfer of energy and cross helicity by about 10% of their respective heating rates. This result agrees qualitatively with solar wind measurements of the energy cascade rate (see Hadid et al. 2017).

   On the other hand, compressible contributions reduce the back transfer of energy, while enhancing the inverse cascade of cross helicity. These compressible contributions can be identified in the classic KHM formulation of the nonlinear transfer of cross helicity as the ones associated with the Laplace force and the divergence of velocity (second and third terms of Equation (7)). Similar terms have been associated with the production of cross helicity in transport models for CMHD (Yokoi 2013). Yet, how these terms translate into real space in a way that benefits the back transfer of cross helicity is unclear. One would expect that compressible fluctuations would be unaffected by the two-dimensionalization of the flow that leads to the back transfers of energy and cross helicity, thus showing the same effect on the nonlinear transfers across all scales. The analysis of KHM terms in CMHD simulations in thin-layer domains could help us better understand the contribution of compressible fluctuations to the direct and inverse cascades.

We conclude that the study of the KHM equations for energy and cross helicity in 3D CMHD simulations has shown that the cascades of both quantities are qualitatively similar in many respects, namely, turbulence anisotropy or the splitting of the cascades and the contribution of compressible fluctuations to the cascade rates. On the other hand, the quantitative differences are striking and their relation to physical phenomena observed in the solar wind and the magnetosphere has been proposed. Thus, the KHM equations are a useful tool that allows for a deeper understanding of turbulent dynamics. In future works, we will extend their use to study the properties of generalized helicity at inertial and kinetic scales.

V.M.-C. is supported by a PPLZ postdoctoral fellowship from the Czech Academy of Sciences. L.F. is supported by the UK Science and Technology Facilities Council (STFC) grant ST/T00018X/1. The authors acknowledge access to CESNET storage facilities provided by the project "e-INFRA CZ" under the program "Projects of Large Research, Development, and Innovations Infrastructures" LM2018140). The authors thank the reviewer for their useful comments and suggestions.

ORCID iDs

Victor Montagud-Camps https://orcid.org/0000-0002-7848-9200
Petr Hellinger https://orcid.org/0000-0002-5608-0834
Andrea Verdini https://orcid.org/0000-0003-4380-4837
Emanuele Papini https://orcid.org/0000-0002-7969-7415
Luca Franci https://orcid.org/0000-0002-7419-0527
Simone Landi https://orcid.org/0000-0002-1322-8712

References

Alexakis, A., & Biferale, L. 2018, PhR, 767, 1
Andrés, N., & Sahraoui, F. 2017, PhRvE, 96, 053205
Andrés, N., Sahraoui, F., Huang, S., Hadid, L. Z., & Galtier, S. 2022, A&A, 661, A116
Banerjee, S., & Galtier, S. 2013, PhRvE, 87, 013019
Banerjee, S., & Galtier, S. 2017, JPhA, 50, 015501
Belcher, J. W., & Davis, L. J. 1971, JGR, 76, 3534
Carbone, V., Sorriso-Valvo, L., & Marino, R. 2009, EL, 88, 25001
Chen, C. H. K., Bale, S. D., Bonnell, J. W., et al. 2020, ApJS, 246, 53
Coburn, J. T., Forman, M. A., Smith, C. W., Vasquez, B. J., & Stawarz, J. E. 2015, RSPTA, 373, 20140150
D'Amicis, R., & Bruno, R. 2015, ApJ, 805, 84
de Karman, T., & Howarth, L. 1938, RSPSA, 164, 192
Dobrowolny, M., Mangeney, A., & Veltri, P. 1980, PhRvL, 45, 144
Frisch, U. 1995, Turbulence: The Legacy of A.N. Kolmogorov (Cambridge: Cambridge Univ. Press)
Galtier, S., Nazarenko, S. V., Newell, A. C., & Pouquet, A. 2000, JPlPh, 63, 447
Grappin, R., Frisch, U., Pouquet, A., & Leorat, J. 1982, A&A, 105, 6
Grappin, R., Müller, W.-C., & Verdini, A. 2016, A&A, 589, A131
Grete, P., O'Shea, B. W., Beckwith, K., Schmidt, W., & Christlieb, A. 2017, PhPl, 24, 092311
Hadid, L. Z., Sahraoui, F., & Galtier, S. 2017, ApJ, 838, 9
Hellinger, P., Papini, E., Verdini, A., et al. 2021, ApJ, 917, 101
Hellinger, P., Verdini, A., Landi, S., et al. 2021, PhRvF, 6, 044607
Huba, J. D. 2005, PhPl, 12, 012322
Iroshnikov, P. S. 1963, AZh, 40, 742
Kida, S., & Orszag, S. A. 1990, JSCom, 5, 85
Kolmogorov, A. N. 1941, DoSSR, 32, 16
Kraichnan, R. H. 1965, PhFl, 8, 1385
Lithwick, Y., Goldreich, P., & Sridhar, S. 2007, ApJ, 655, 269
MacBride, B. T., Smith, C. W., & Forman, M. A. 2008, ApJ, 679, 1644
Marino, R., Sorriso-Valvo, L., D'Amicis, R., et al. 2012, ApJ, 750, 41
Meyrand, R., Kiyani, K. H., & Galtier, S. 2015, JFM, 770, R1
Mininni, P. D., & Pouquet, A. 2009, PhRvE, 79, 026304
Monin, A. S., & Iaglom, A. M. 1975, Statistical Fluid Mechanics: Mechanics of Turbulence (Cambridge, MA: MIT Press)
Montagud-Camps, V., Grappin, R., & Verdini, A. 2020, ApJ, 902, 34
Morize, C., Moisy, F., & Rabaud, M. 2005, PhFl, 17, 095105
Musacchio, S., & Boffetta, G. 2017, PhFl, 29, 111106
Podesta, J. J. 2011, PhPl, 18, 012907
Politano, H., & Pouquet, A. 1998, PhRvE, 57, R21
Pritchett, P. L., & Coroniti, F. V. 2004, JGRA, 109, A01220
Shi, C., Velli, M., Panasenco, O., et al. 2021, A&A, 650, A21
Smith, C. W., Stawarz, J. E., Vasquez, B. J., Forman, M. A., & MacBride, B. T. 2009, PhRvL, 103, 201101
Smith, C. W., Vasquez, B. J., Coburn, J. T., Forman, M. A., & Stawarz, J. E. 2018, ApJ, 858, 21
Sorriso-Valvo, L., Marino, R., Carbone, V., et al. 2007, PhRvL, 99, 115001
Stawarz, J. E., Smith, C. W., Vasquez, B. J., Forman, M. A., & MacBride, B. T. 2009, ApJ, 697, 1119
Stawarz, J. E., Smith, C. W., Vasquez, B. J., Forman, M. A., & MacBride, B. T. 2010, ApJ, 713, 920
Telloni, D., D'Amicis, R., Bruno, R., et al. 2021, ApJ, 916, 64
Tharp, T. D., Yamada, M., Ji, H., et al. 2013, PhPl, 20, 055705
Vasquez, B. J., Forman, M. A., Coburn, J. T., Smith, C. W., & Stawarz, J. E. 2018, ApJ, 867, 156

Vasquez, B. J., Smith, C. W., Hamilton, K., MacBride, B. T., & Leamon, R. J. 2007, JGRA, 112, A07101
Verdini, A., Grappin, R., Hellinger, P., Landi, S., & Müller, W. C. 2015, ApJ, 804, 119
Verdini, A., Grappin, R., Montagud-Camps, V., et al. 2019, NCimC, 42, 17
Widmer, F., Büchner, J., & Yokoi, N. 2016, PhPl, 23, 042311
Wray, A. A. 1990, Minimal storage time-advancement schemes for spectral methods, MS 202 A-1, NASA Ames Research Center, CA
Yokoi, N. 2011, JTurb, 12, N27
Yokoi, N. 2013, GApFD, 107, 114
Yokoi, N., & Balarac, G. 2011, JPhCS, 318, 072039
Zank, G. P., Adhikari, L., Hunana, P., et al. 2017, ApJ, 835, 147